MATERIALS SCIENCE

General and programmable synthesis of hybrid liposome/metal nanoparticles

Jin-Ho Lee,[1,2]* Yonghee Shin,[1]* Wooju Lee,[3] Keumrai Whang,[1] Dongchoul Kim,[3] Luke P. Lee,[2] Jeong-Woo Choi,[1] Taewook Kang[1]†

Hybrid liposome/metal nanoparticles are promising candidate materials for biomedical applications. However, the poor selectivity and low yield of the desired hybrid during synthesis pose a challenge. We designed a programmable liposome by selective encoding of a reducing agent, which allows self-crystallization of metal nanoparticles within the liposome to produce stable liposome/metal nanoparticles alone. We synthesized seven types of liposome/monometallic and more complex liposome/bimetallic hybrids. The resulting nanoparticles are tunable in size and metal composition, and their surface plasmon resonance bands are controllable in visible and near infrared. Owing to outer lipid bilayer, our liposome/Au nanoparticle shows better colloidal stability in biologically relevant solutions as well as higher endocytosis efficiency than gold nanoparticles without the liposome. We used this hybrid in intracellular imaging of living cells via surface-enhanced Raman spectroscopy, taking advantage of its improved physicochemical properties. We believe that our method greatly increases the utility of metal nanoparticles in in vivo applications.

INTRODUCTION

Metal nanoparticles have been extensively used in a wide range of biomedical applications, such as those in labeling and probing, because of their unique physical and chemical properties (1–12). However, their in vivo applications are often limited because of their weak colloidal stability and poor endocytosis efficiency (13, 14). To overcome these limitations, hybrid structures have been created by using various biocompatible organic materials to improve their physicochemical properties, especially colloidal stability in biological environments (15–20). In this regard, liposomes have attracted much attention, because the lipid bilayer can drastically increase the colloidal stability and efficiency of intracellular delivery of the resulting hybrid structure (20–30).

Hybrids of liposomes and metal nanoparticles have been prepared through several approaches. A thin film of lipid bilayer is hydrated to form a liposome, which may happen to simultaneously encapsulate colloidal nanoparticles during the formation of the liposome if there are metal nanoparticles nearby. This method generally suffers from low yield and poor selectivity of the hybrids. In addition, removal of free metal nanoparticles (that is, metal nanoparticles that are not encapsulated) and free liposomes (that is, liposomes that do not contain metal nanoparticles) must be done carefully through additional separations (25–27). On the other hand, metal nanoparticles can also be embedded between lipid bilayers or, alternatively, can be attached to the outer liposome surface through delicate control of their surface chemistry (21, 23, 28–30). However, for both methods, the metal nanoparticles should be small enough to produce a stable hybrid structure without degrading the structural integrity of the lipid bilayer. For example, embedded metal nanoparticles larger than ca. 6.5 nm may disrupt the lipid bilayer, resulting in micelle formation (21, 28, 30, 31). The attachment of the nanoparticles onto the surface of the outer lipid often leads to leakage of the liposome structure (32). Occasionally, the attached nanoparticles would bridge other adjacent liposomes by electrostatic attraction, which might result in aggregation of the liposomes depending on the number ratio of nanoparticle to liposome (33, 34). It is well known that surface plasmon resonance (SPR) band is strongly damped for small metal nanoparticles. Hence, a novel method that produces stable hybrids of liposomes and metal nanoparticles with high selectivity is highly desirable.

Here, we propose a general and facile synthetic strategy for liposome/metal hybrid nanoparticles by designing programmable liposomes. In these programmable liposomes, a reducing agent is encoded to allow the selective self-crystallization of various metal nanoparticles inside the liposome via rapid diffusion of metal precursor complexes across lipid bilayers. The generality and versatility of our proposed method are demonstrated by the wide variety of liposome/metal hybrids it produces. The colloidal stability and efficiency of the intracellular delivery of our liposome/metal hybrid nanoparticles were investigated by using liposome/Au hybrid nanoparticles (LGNP). Intracellular imaging of living cells via surface-enhanced Raman spectroscopy (SERS) was also carried out. Our method has several key advantages over previous approaches (fig. S1). First, it produces, in principle, only the desired liposome/metal hybrid nanoparticles without additional separation steps. Second, the resulting hybrids are tunable in size and metal composition. Their SPR bands are also controllable in visible and near-infrared range. Third, the structural integrity of the lipid bilayer of the resulting hybrid is highly stable during synthesis. These factors contribute to the physicochemical properties of the hybrid nanoparticles, such as colloidal stability and efficiency of intracellular delivery.

RESULTS

Programmable and facile synthesis of various liposome/metal hybrid nanoparticles

A schematic illustration of the programmable synthesis of the liposome/metal hybrid nanoparticles is presented in Fig. 1. To selectively encode the reducing agent in the liposome (Fig. 1A), the lipid bilayer is hydrated by an aqueous solution of the reducing agent and then separated through a polycarbonate membrane filter to obtain unilamellar liposomes with uniform size (30 to 200 nm). The liposomes encoded with the reducing agent are collected by centrifugation to remove the remaining

[1]Department of Chemical and Biomolecular Engineering, Sogang University, Seoul 121-742, Korea. [2]Biomolecular Nanotechnology Center, Berkeley Sensor and Actuator Center, Department of Bioengineering, University of California, Berkeley, Berkeley, CA 94720, USA. [3]Department of Mechanical Engineering, Sogang University, Seoul 121-742, Korea.
*These authors contributed equally to this work.
†Corresponding author. Email: twkang@sogang.ac.kr
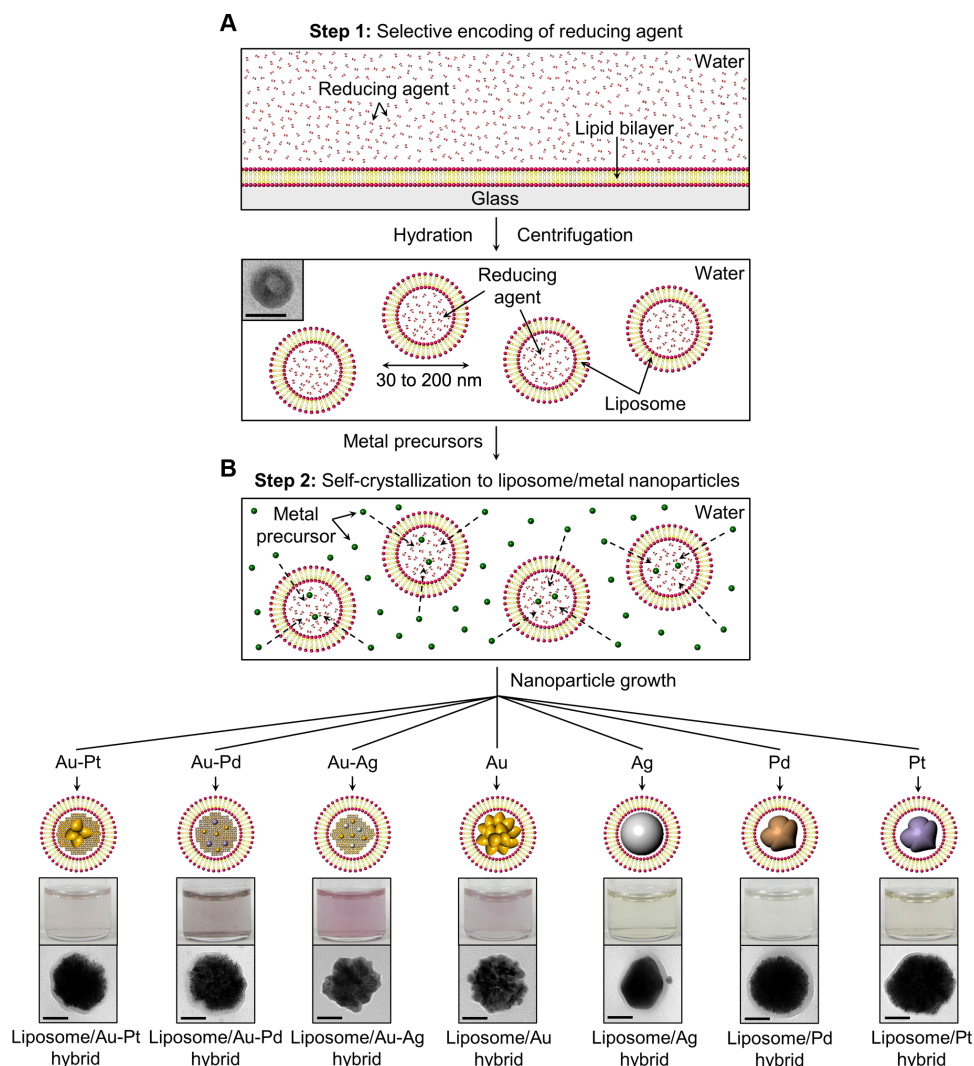
Fig. 1. Programmable and facile synthesis of various liposome/metal hybrid nanoparticles. (A and **B)** Schematic illustration of selective encoding of a reducing agent in a liposome [step 1 (A)] and spontaneous crystallization of metal precursors into metal nanoparticles inside the liposome through the diffusion of the metal precursors [step 2 (B)]. Bottom two photos correspond to the photographs of the resulting hybrid solutions and representative TEM images for the as-made hybrid particles. Scale bars, 50 nm.

reducing agent. To allow the self-crystallization of metal nanoparticles inside the liposome (Fig. 1B), the encoded liposomes are redispersed in an aqueous solution of the metal precursor. The metal precursor quickly diffuses into the liposome, and then the metal precursor inside the liposome undergoes reduction to the metal nucleus. Eventually, the nucleus grows into a metal nanoparticle, producing only the liposome/metal hybrid nanoparticle in solution. Depending on the metal precursor (that is, Au, Ag, Pd, Pt, Au-Ag, Au-Pd, and Au-Pt precursors), various liposome/metal hybrid nanoparticles can be selectively synthesized through our proposed method (Fig. 1B, bottom).

Self-crystallization of gold nanoparticles in liposomes containing the reducing agent

Liposomes encoded with the reducing agent were prepared by using 1,2-distearoyl-*sn*-glycero-3-phosphocholine (DSPC) as lipid and trisodium citrate as reducing agent. Liposomes were extruded through membrane filters with different pore sizes (30, 50, 100, and 200 nm). To characterize the as-prepared liposomes after filtration, transmission electron microscopy (TEM) measurements were carried out. Figure 2A

shows representative TEM images of the liposomes. To statistically analyze their sizes, 45 liposomes in the TEM images were randomly selected. The average sizes of the liposomes are found to be 37.6 ± 7.4, 55.0 ± 14.6, 104.5 ± 24.7, and 197.7 ± 58.6 nm (respectively corresponding to pore sizes of 30, 50, 100, and 200 nm; Fig. 2, C and D).

After the addition of gold precursor ($HAuCl_4 \cdot 3H_2O$) to the aqueous solution with the reducing agent–encoded liposome, the color of the resulting cloudy mixture gradually changed to pink. The mixture was then sampled for TEM measurements. The TEM images show nanoparticles with a thin outer lipid layer (Fig. 2B and fig. S2), which is indicative of nanoparticle growth inside the liposome. To ensure selective growth inside the liposome, two control experiments were carried out. No color change is observed after the addition of gold precursor to the aqueous solution having the liposome without the reducing agent (fig. S3A). No apparent SPR band is observed in the absorbance spectrum of the solution (fig. S3B). Moreover, the addition of gold precursor to the reducing agent alone (the concentration of the reducing agent was adjusted to 3 μM to match closely the concentration outside the reducing agent–encoded liposome) also produces nearly identical results (that is,
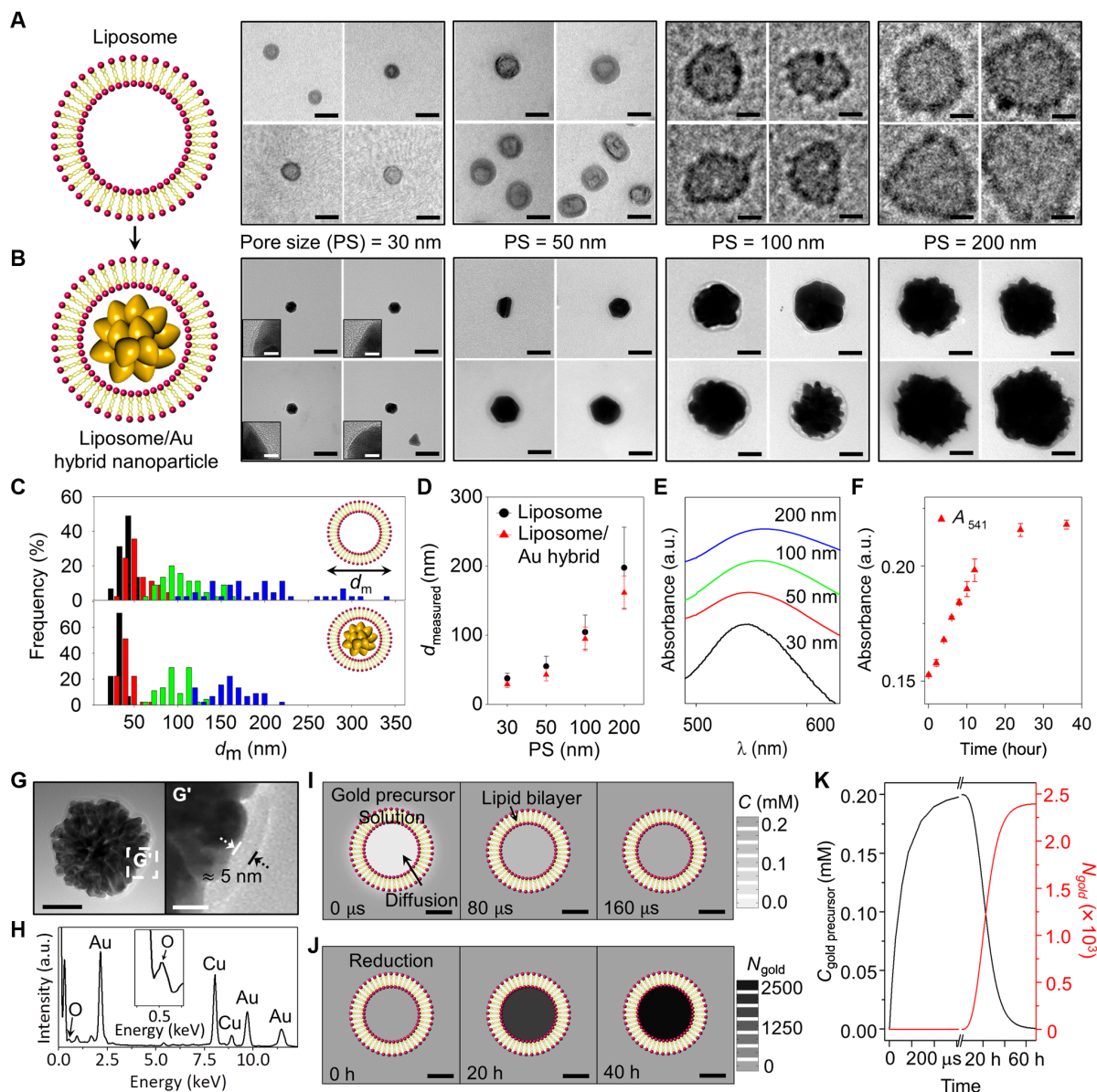
Fig. 2. Self-crystallization of GNP in a reducing agent–encoded (LGNP). (**A** and **B**) Representative TEM images of liposomes (A) and resulting LGNP (B) according to filter pore size (30, 50, 100, and 200 nm). (**C** and **D**) Size distributions (C) and relation (D) between the liposomes and the LGNP. (**E**) Representative absorbance spectra of the LGNP solutions with different sizes. a.u., arbitrary units. (**F**) Plot of absorbance at SPR peak (541 nm) of the LGNP as a function of time. (**G** and **H**) Representative TEM image (G) and EDS spectrum (H) of the LGNP prepared by using ascorbic acid as another reducing agent. (**I**) Concentrations of gold precursor in the liposome due to diffusion after 0, 80, and 160 μs. (**J**) The number of gold atoms in the liposome due to reduction after 0, 20, and 40 hours. (**K**) Concentration of gold precursor (black) and the number of gold atoms (red) inside the liposome as a function of time. Scale bars, 50 nm (A, B, and G) and 10 nm [insets in (B), (G′), (I), and (J)].

neither color change nor SPR band; fig. S3, C and D). In each TEM image, 45 hybrid particles were randomly selected, and their sizes were statistically analyzed. The average sizes of the particles are 28.9 ± 4.6, 42.8 ± 8.9, 94.6 ± 17.0, and 161.6 ± 24.2 nm (respectively corresponding to pore sizes of 30, 50, 100, and 200 nm), which are slightly smaller than the size of the liposomes; however, their size distributions are similar to those of the liposomes (Fig. 2, C and D). Absorbance spectra of all resulting solutions show distinct SPR bands (Fig. 2E). The SPR band becomes broader and red-shifts from 541 to 563 nm with the increasing pore size of the filter (Fig. 2E), consistent with the TEM results. To estimate the formation kinetics of gold nanoparticles inside the reducing agent–encoded liposome, ultraviolet (UV)–visible absorbance

spectra were obtained over time. Two hours after the addition of gold precursor, an SPR band appears at 541 nm (Fig. 2F). The intensity gradually increases and becomes saturated after around 24 hours (Fig. 2F). Note that the reduction of gold ions above the transition temperature of the lipid (DSPC; 55°C) generates gold nanoparticles without the lipid bilayer (fig. S4). Ascorbic acid was also tested to determine whether our method works with another reducing agent. The experiment using ascorbic acid produces LGNP identical to those produced with trisodium citrate (Fig. 2G). For example, the magnified TEM image marked by G′ in Fig. 2G shows an outer lipid layer with a thickness of ca. 5 nm, which is consistent with the length of the lipid bilayer (35). The spectrum of the resulting particles, which is obtained by energy-dispersive x-ray

spectroscopy (EDS), shows several peaks that are assigned to the gold atom (Fig. 2H). The peak corresponding to the oxygen atom is also apparent in the EDS spectrum (Fig. 2H), supporting the existence of the outer lipid (DSPC) bilayer (fig. S5 and table S1). The absorbance spectra show a noticeable SPR band after 0.5 hours, which gradually red-shifts (that is, 572 to 594 nm after 10 hours; fig. S6).

It is known that only small, uncharged molecules can diffuse into a liposome across a lipid bilayer because of the amphipathic property of lipids (36). Multiple gold ion complexes can coexist when gold precursor is dissolved in water, depending on the solution pH (37). We postulate that the neutral forms of the possible gold ion complexes (for example, $AuCl_3 \cdot H_2O$) can diffuse across the lipid bilayer into the liposome. To test this hypothesis and to estimate diffusion kinetics, three-dimensional (3D) simulations were performed. Local concentrations of the gold precursor (that is, neutral gold ion complex) and the gold atom [that is, Au(0)] were calculated through the following reaction-diffusion equation

$$\frac{\partial c_i}{\partial t} = \nabla \cdot (D_i \nabla c_i) + k_i c_1 c_2^{2/3} \qquad (1)$$

where c_i, D_i, and k_i are the concentration, diffusivity, and rate constant of the ith species, respectively. The subscription index ($i = 1$ or 2) corresponds to the neutral gold ion complex and gold atom, respectively. This equation considers both the diffusion flux of the neutral gold ion complex into the liposome and the reaction rate for the reduction of Au(1) to Au(0) (38–40). Because molecules have diffusive properties that depend on the solvent, the diffusivity of the neutral gold ion complex in water is different from that in the lipid bilayer (fig. S7) (38, 39). The reduction rate inside the liposome was assumed to be equivalent to the rate of gold ion reduction by citrate (40). Further details of the simulations are described in the Supplementary Materials. The concentration of the neutral gold ion complex and the number of gold atoms inside the liposome as functions of time are shown in Fig. 2 (I to K). The concentration of the neutral gold ion complex in the liposome rapidly increases, reaching that of the neutral gold ion complex outside the liposome over a short period of time (240 μs; Fig. 2K, black line). On the other hand, the number of gold atoms gradually increases and saturates after 40 hours (Fig. 2K, red line). This simulation result is in agreement with the UV-visible absorbance results for the formation kinetics of gold nanoparticles in the liposome. Note that the lipid bilayer prevents diffusion of large molecules [for example, the reducing agents (trisodium citrate and ascorbic acid) that we used] into a liposome. When we tried a reversed method to generate hybrid particles (that is, to encapsulate metal ions first and then to diffuse the reducing agents into the liposomes), as expected, neither color change nor SPR band is observed (fig. S8).

Extension of the programmable synthesis to the selective synthesis of other liposome/metal hybrid nanoparticles

To test the versatility of our proposed programmable synthesis, other metal precursors [namely, silver (Ag), palladium (Pd), and platinum (Pt)] were used. Except for the metal precursor, the experimental conditions were identical to those for the liposome/Au hybrids. In all cases, color changes after the addition of the metal precursors were observed. For example, the solution turns yellow, and an SPR band appears between 400 and 500 nm after the addition of the Ag precursor to the aqueous solution containing the reducing agent–encoded liposome (fig. S10A). Representative TEM images show that the nanoparticles are located in the liposomes (Fig. 3, A to C). The average sizes of the resulting hybrid nanoparticles are found to be 102.9 ± 22.5 nm (liposome/

Ag hybrid), 109.4 ± 35.6 nm (liposome/Pd hybrid), and 99.3 ± 20.0 nm (liposome/Pt hybrid) (fig. S11). Note that the amounts of metal atoms in the resulting hybrid solutions (that is, liposome/Au, liposome/Ag, and liposome/Pd hybrids), measured by inductively coupled plasma atomic emission spectroscopy, are found to be similar (table S2).

Simultaneous addition of multiple precursors to the aqueous solution containing the reducing agent–encoded liposome was also studied (that is, Au-Ag, Au-Pd, or Au-Pt precursor mixtures). Representative TEM images for the resulting liposome/Au-Ag, liposome/Au-Pd, and liposome/Au-Pt hybrids are shown in Fig. 3 (D to F). Liposome/Au-Pd and liposome/Au-Pt hybrids are highly branched. Each magnified TEM image (D′ in Fig. 3D, E′ in Fig. 3E, and F′ in Fig. 3F) suggests the existence of an outer lipid layer around the nanoparticles. On average, the sizes of the resulting liposome/Au-Ag, liposome/Au-Pd, and liposome/Au-Pt hybrids are 93.6 ± 21.0, 104.9 ± 35.0, and 93.3± 27.3 nm, respectively (fig. S11). Peaks corresponding to Au and Ag atoms are present in the EDS spectrum of the liposome/Au-Ag hybrid nanoparticle (fig. S12A), proving that the resulting particle is bimetallic. Au-Pd and Au-Pt precursor combinations also produce bimetallic liposome hybrids (fig. S12, B and C). These results indicate that our method can be easily extended to the selective synthesis of various liposome/metal hybrid nanoparticles.

To further examine the elemental distribution in single-liposome/bimetallic hybrid nanoparticles, EDS elemental maps and line profiles for each hybrid nanoparticle were obtained. Figure 3G shows a TEM image of liposome/Au-Ag hybrid nanoparticles and the corresponding elemental maps of Au and Ag, which indicate the uniform distribution of both elements. The compositional line profile is also consistent with elemental maps (fig. S13A). Similar to those in the liposome/Au-Ag hybrid, Au and Pd atoms are uniformly distributed throughout the hybrid (Fig. 3H and fig. S13B). On the other hand, the elemental map and line profile of Au and Pt for the liposome/Au-Pt hybrids show that the Au atoms are more abundant around the core of the particle, whereas both atoms are distributed evenly near the periphery of the particle (Fig. 3I and fig. S13C). For crystallographic analysis, we further characterized the bimetallic hybrid nanoparticles by aberration-corrected TEM (CS-TEM). Figure 3J shows representative CS-TEM images of the liposome/Au-Ag hybrid nanoparticles. Most of the measured lattice spacings are 0.236 nm (1 in Fig. 3J), which match the d-spacing (0.236 nm) for the (111) plane of Au-Ag bimetallic alloy (41). Notably, spacings corresponding to those for the (111) plane of Au crystal (0.235 nm) (42) and Ag crystal (0.238 nm) (43) are also observed in a smaller region of a particle (2 in Fig. 3J). The lattice spacings of the liposome/Au-Pd hybrid nanoparticle (Fig. 3K) are found to be 0.231, 0.235, and 0.224 nm, which correspond to the (111) planes of Au-Pd alloy (44), Au crystal (42), and Pd crystal (44), respectively. Lattice spacings for the liposome/Au-Pt hybrid correspond to the coexisting (200) plane (0.195 nm; 1 in Fig. 3L) and (111) plane (0.224 nm; 2 in Fig. 3L) of the Pt crystal (45). Additionally, the d-spacing for the (111) plane of the Au-Pt alloy is observed (0.230 nm; 2 in Fig. 3L) (46).

It is known that the optical property of the bimetallic nanoparticles is tunable within the visible and near-infrared region by changing their composition. To control the SPR bands of the resulting bimetallic hybrid nanoparticles, we further attempted to vary their composition by changing the molar ratios of their two metal precursors. As shown in fig. S14, the morphologies of the resulting liposome/bimetallic hybrids are unchanged in all cases irrespective of the molar ratios of metal precursors. To examine the change in composition of the hybrids with respect to the precursor ratio, the atomic percentage of each metal
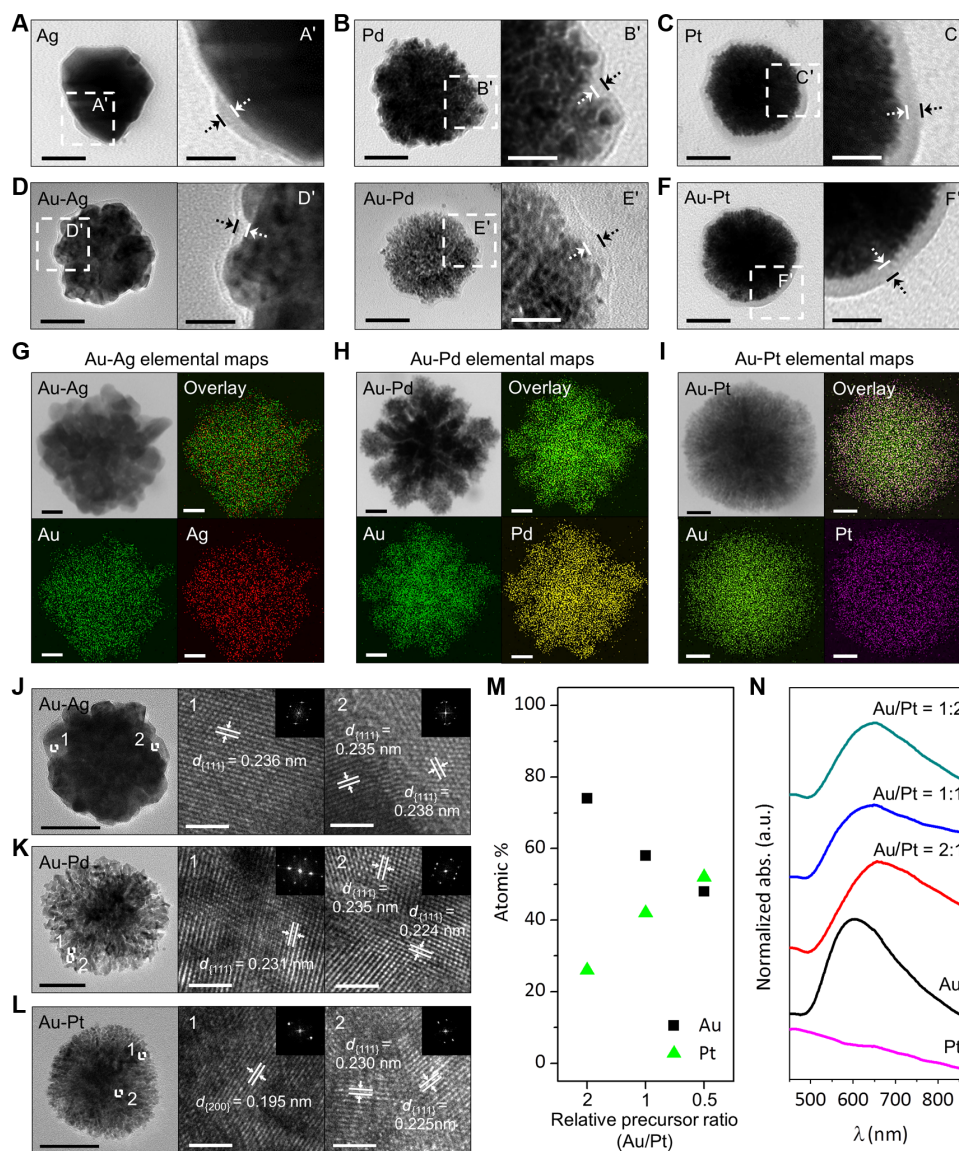
Fig. 3. Extension of our proposed programmable synthesis to the selective synthesis of a wide variety of liposome/metal hybrids. (**A** to **C**) Representative TEM images of liposome/monometallic hybrids [Ag (A), Pd (B), and Pt (C)]. (**D** to **F**) Representative TEM images of liposome/bimetallic hybrids [Au-Ag (D), Au-Pd (E), and Au-Pt (F)]. (**G** to **I**) Representative TEM images and corresponding EDS element maps of the liposome/bimetallic hybrids [Au-Ag (G), Au-Pd (H), and Au-Pt (I)]. (**J** to **L**) Representative CS-TEM images, lattice-resolved images (numbered boxes), and electron diffraction patterns (the insets of the numbered boxes) of liposome/bimetallic hybrids [Au-Ag (J), Au-Pd (K), and Au-Pt (L)]. (**M** and **N**) Atomic percentages (M) and absorbance spectra (N) of liposome/Au-Pt hybrids synthesized from the precursor molar ratios of 2:1 (Au/Pt), 1:1, and 1:2. Scale bars, 50 nm (A to F and J to L), 20 nm (A' to F', and G to I), and 2 nm [numbered boxes in (J), (K), and (L)].

element was calculated from the EDS spectrum. The atomic percentage of the hybrid particle is linearly proportional to the molar ratio of each precursor. For instance, the atomic percentage of Pt in the liposome/Au-Pt hybrid nanoparticles is almost twofold and increases to twice the molar ratio of the Pt precursor (from 26 to 52%; Fig. 3M). Similar tendencies are observed with both liposome/Au-Ag and liposome/Au-Pd hybrid nanoparticles (fig. S15, A and C). The color change in the resulting solution of the liposome/bimetallic hybrid is also noteworthy. For example, the resulting liposome/Au-Pt hybrid solution was reddish brown, whereas the liposome/Au hybrid and liposome/Pt hybrid particle solutions were pink and yellowish brown, respectively. The optical properties of liposome/bimetallic hybrid nanoparticles with different elemental compositions were investigated by measuring their

UV-visible absorbance. Generally, bimetallic alloys have a broad SPR band instead of two distinct SPR bands that come from individual metal nanoparticles. The resulting bimetallic hybrids exhibit broad SPR bands, consistent with the elemental and crystallographic analysis results. The SPR peak for the liposome/Au-Pt hybrid red-shifts from 604 to 647 nm as the SPR bandwidth broadens with increasing molar ratio of the Pt precursor (Fig. 3N). This change may be attributed to surface plasmon coupling between Au and Pt (47). On the other hand, the absorbance spectrum of the liposome/Au-Ag hybrid that exhibits the SPR band, which slightly blue-shifts from 600 to 570 nm as the molar ratio of the Ag precursor, increases (fig. S15B) because of the increase in the Ag content of the alloy (48). The additional plasmon band for the liposome/Au-Pd hybrid in the near-infrared region appears with
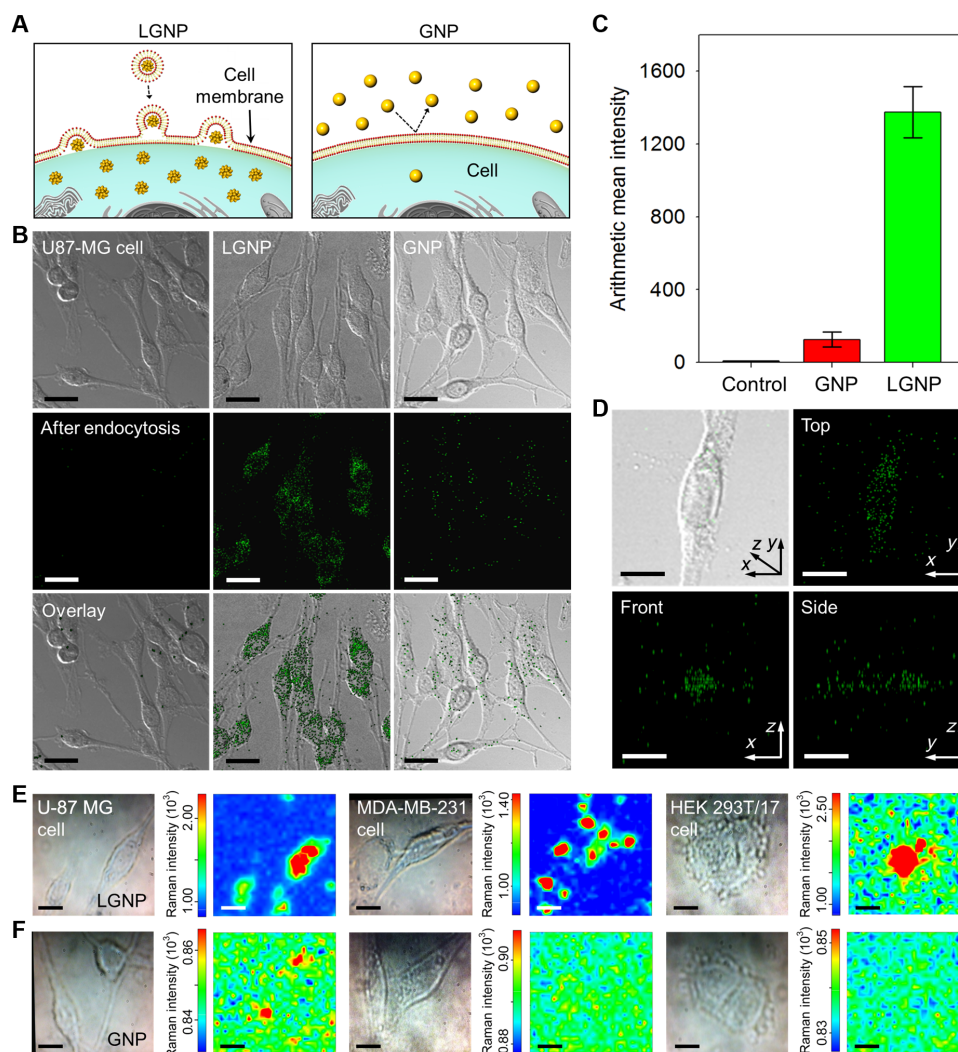
Fig. 4. Analysis of endocytosis efficiency of LGNP and intracellular imaging via SERS. (**A**) Schematic representation for cellular uptake of LGNP and GNP. (**B**) Comparison of endocytosis efficiency using U-87 MG cells with a confocal microscope. First row: Differential interference contrast image; second row: scattering image; third row: overlay image. First column: Cells only; second column: LGNP; third column: GNP. (**C**) Mean signal intensity per single cell from control (cells only) (7.2 ± 1.8), GNP (125.9 ± 41.3), and LGNP (1374.8 ± 141.6). (**D**) 3D analysis of the intracellular distribution of LGNP in the single cell. (**E** and **F**) Optical microscope images and Raman maps obtained from U-87 MG, MDA-MB-231, and HEK 293T/17 cells after being treated with LGNP (E) and GNP (F). Scale bars, 10 μm (B and D to F).

the increase in molar ratio of the Pd precursor (fig. S15D). The resonance in the near-infrared region may be due to strong coupling of the collective oscillation of conduction electrons to the interband transitions between Au and Pd atoms (*10*).

Improved efficiency of endocytosis of LGNP

In general, nanoparticles must maintain colloidal stability under physiological conditions. To investigate the colloidal stability of our LGNP, we incubated LGNP with various biologically relevant solutions. Control experiments using bare gold nanoparticles (GNP) and gold nanorods (GNR) were also carried out. To analyze the long-term colloidal stability, we measured the changes in absorbance for the SPR band for each LGNP (541 nm), GNP (571 nm), and GNR (786 nm) solutions that were incubated at 4°C over time (from 1 min to 1 month). The absorbance intensities of GNP and GNR are substantially decreased after mixing with most of the solutions under study, except human serum (fig. S16A). In contrast, the absorbance intensity of LGNP in all solutions does not

change (fig. S16A), staying approximately above 80% even after 1 month of incubation (fig. S16B). This enhanced colloidal stability of the resulting hybrid may be attributed to steric repulsion by the lipid layer of neighboring hybrids (*49*) and to zwitterionic characteristics of the head group of the lipid, which can carry charges over a wide pH range (*50*).

To analyze for an increase in efficiency of LGNP endocytosis due to the stable outer lipid layers, we applied LGNP and GNP (ca. 10^8 particles/ml) to *Homo sapiens* brain glioblastoma U-87 MG cells (ca. 2×10^5 cells/ml) (Fig. 4A). The viabilities of the cells treated with LGNP and GNP solutions were examined by MTT [3-(4,5-dimethylthiazol-2-yl)-2,5-diphenyltetrazolium bromide] assay because residual materials (that is, GNP without lipid bilayer, Au ions, etc., which may coexist in the solutions) might affect cell viability. More than ca. 99% of the cells remain viable in LGNP solution with a concentration of ca. 10^8 particles/ml (fig. S17), showing that the effect of the LGNP solution on cell viability is negligible. The cellular uptake of these nanoparticles was indirectly investigated by the measurement of scattering signals from the cells

Lee *et al. Sci. Adv.* 2016;**2**:e1601838   16 December 2016

6 of 9

after they were separately treated with the nanoparticles. No apparent scattering signal is observed with U-87 MG cells without the particles (first column in Fig. 4B). An intense scattering signal is observed from the cells incubated with LGNP (second column in Fig. 4B), whereas a much weaker signal is obtained with GNP (third column in Fig. 4B). For statistical analysis, the mean scattering signal per cell was calculated by considering the overall number of signal frequencies obtained within the wavelength range of 548 to 671 nm. The calculated mean intensity per single cell with LGNP (1367.6 ± 141.6) is more than 10 times greater than that per single cell with GNP (118.6 ± 41.3) (Fig. 4C), strongly supporting the improved efficiency of endocytosis of the hybrid nanoparticles. The distribution of LGNP in each cell was further analyzed through 3D imaging (40 z-stack images) using a confocal microscope. Overlapping optical differential interference contrast images and scattering signals (Fig. 4D) show that LGNP is uniformly dispersed in the cytoplasmic region.

Intracellular imaging of living cells via SERS

To determine the advantages of the improved efficiency of intracellular delivery and colloidal stability of the hybrid particles, intracellular SERS was used as a proof of concept. Three different cell lines obtained from *H. sapiens* brain glioblastoma (U-87 MG; ca. 2×10^5 cells/ml), breast epithelium (MDA-MB-231; ca. 2×10^5 cells/ml), and kidney [human embryonic kidney (HEK) 293T/17; ca. 2×10^5 cells/ml] were treated with LGNP and GNP (ca. 10^8 particles/ml) on transparent glass substrates. Different characteristic Raman transitions are observed with each cell line treated with LGNP (red, green, and blue lines in fig. S18). However, no apparent Raman transition could be found in the Raman spectra of GNP-treated cells (black line in fig. S18). Because Raman transitions were obtained from three different spots, Raman imaging was conducted for each cell line with notable overlapping Raman transitions in various ranges (U-87 MG, 600 to 700 cm^{-1}; MDA-MB-231, 1060 to 1070 cm^{-1}; HEK 293T/17, 1000 to 1100 cm^{-1}; red bars in fig. S18). Raman maps for LGNP-treated cell lines show clear images that are consistent in shape and position with the optical microscopy images (Fig. 4E). In contrast, no clear Raman images from GNP-treated cells were obtained (Fig. 4F).

To determine whether the observed signals originated from intracellular structures, we fixed U-87 MG cells exposed to LGNP and GNP with formaldehyde and treated them with fluorescent dye (Alexa Fluor 546) to stain their cytoskeleton (F-actin). No notable Raman transitions in cells treated with GNP and the dye were observed even after a 10-s exposure to laser (fig. S19C). However, the characteristic Raman transition of the dye that does not overlap with the Raman transitions of the cell (734 cm^{-1}; marked by red asterisks in fig. S19A) is enhanced in the cell line incubated with LGNP. In addition, the Raman map created by using the Raman transition of the dye shows a clear intracellular image. Notably, the region that corresponds to the cell nucleus shows no Raman transition (fig. S19B).

DISCUSSION

In conclusion, we have demonstrated the synthesis of hybrid liposome/metal nanoparticles via self-crystallization of metal nanoparticles within programmable liposomes. Because the reducing agent is selectively encoded in the liposome, our method produces liposome/metal hybrid nanoparticles alone without requiring any separation steps. The generality and versatility of our proposed method allow the design of seven types of liposome/monometallic and more complex liposome/bimetallic hybrid nanoparticles without tailoring the surface chemistry of colloidal metal nanoparticles. The formation of the hybrid nanoparticle is confirmed by TEM measurements, EDS analysis, and computational simulation. The size of the hybrid nanoparticles can be tuned to within 30 to 200 nm according to the liposome size. Their SPR bands are also controllable in visible and near-infrared ranges according to the metal composition. The composition of the bimetallic hybrid nanoparticles can be tuned by changing the molar ratio of their two metal precursors. The colloidal stability of LGNP is maintained in various biologically relevant solutions. LGNP also shows higher endocytosis efficiency than GNP without the outer lipid bilayer. These improved physicochemical properties of our hybrid nanoparticles allow their utilization in intracellular imaging of various cell lines via SERS. We strongly believe that our novel method will significantly expand the utility of metal nanoparticles, creating new opportunities in a wide variety of applications, ranging from diagnosis to therapy, especially in intracellular signaling and in vivo imaging.

MATERIALS AND METHODS

Self-crystallization of gold nanoparticles in the liposome that contains a reducing agent

Unilamellar liposome vesicles were prepared by a conventional procedure including the extrusion of multilamellar vesicles. A chloroform solution with 500 µg of saturated neutral phospholipids (DSPC) was poured into a round vial, and a multilayered lipid film was formed by evaporating the chloroform under nitrogen stream. The film was held under vacuum over 1 hour and then hydrated at 55°C by adding 1 ml of reducing agent solution [that is, 300 mM trisodium citrate dihydrate ($Na_3C_6H_5O_7 \cdot 2H_2O$) (pH 2.0) or 300 mM ascorbic acid ($C_6H_8O_6$) (pH 5.0)]. To obtain homogeneous unilamellar liposome vesicles, the produced liposomes were passed through a polycarbonate membrane with a specific pore size (30, 50, 100, and 200 nm in diameter) 25 times at 60°C using a mini-extruder (Avanti Polar Lipids). The unilamellar liposomes were separated by centrifugation at 16,400g for 15 min at 15°C by using a 1.5-ml microcentrifuge tube and washed with deionized water three times to remove the remaining residues. The liposomes encoded with the reducing agent were resuspended in 1 ml of gold precursor [200 µM tetrachloroauric acid trihydrate ($HAuCl_4 \cdot 3H_2O$)] aqueous solution and kept in a shaking incubator at room temperature overnight to synthesize LGNP.

Programmable synthesis for other liposome/metal hybrid nanoparticles

For the synthesis of the liposome/monometallic hybrid nanoparticles, the liposomes encoded with the reducing agent were redispersed in metal precursor aqueous solution, such as silver nitrate ($AgNO_3$), potassium tetrachloropalladate(II) (K_2PdCl_4), and chloroplatinic acid hydrate ($H_2PtCl_6 \cdot xH_2O$) and kept in a shaking incubator at room temperature overnight. For the synthesis of the liposome/bimetallic hybrid nanoparticles, mixtures of Au and Ag precursors, Au and Pd precursors, or Au and Pt precursors were introduced in the liposomes containing the reducing agent solution. Then, the solution was kept in a shaking incubator at room temperature overnight.

TEM and UV-visible absorbance measurement

As-prepared liposomes (10 µl) and the resulting liposome/metal hybrid nanoparticles solutions were dropped onto a carbon-coated 300 mesh TEM grid (Ted Pella Inc.) for TEM analysis. TEM images were obtained

with a Carl Zeiss LIBRA 120 electron microscope operating at an acceleration voltage of 120 kV. The UV-visible absorbance spectra were taken by JASCO V-530 UV spectrometer.

EDS and crystallographic analysis
EDS and crystallographic studies were performed in a JEOL JEM-ARM200F electron microscope operating at an acceleration voltage of 200 kV. TEM samples were prepared by carefully dropping 10 μl of the resulting liposome/bimetallic hybrid nanoparticles solutions onto a carbon-coated 300 mesh TEM grid (Ted Pella Inc.).

Cell culture
The *H. sapiens* brain glioblastoma U-87MG cells, *H. sapiens* epithelial breast MDA-MB-231 cells, and *H. sapiens* kidney HEK 293T/17 cells (American Type Culture Collection) were maintained in high-glucose Dulbecco's modified Eagle's medium (DMEM) (LM 001-07, Welgene), RPMI 1640 medium (LM 011-01, Welgene), and high-glucose DMEM (ATCC 30-2002, American Type Culture Collection) supplemented with 10% fetal bovine serum (S1520, Biowest) and 1% penicillin/streptomycin (Gibco, Invitrogen), respectively. Cell cultures were incubated at 37°C and equilibrated in 5% CO_2 and air.

Cell viability test based on MTT assay
Before cell treatment, as-prepared LGNP and GNP solutions were centrifuged at 6000*g* for 10 min and then redispersed in phosphate-buffered saline (PBS) buffer solution [PBS 1× (pH 7.4)]. U-87 MG cells (ca. 10^4 cells/ml) were incubated with LGNP and GNP (ranging from 10^7 to 10^9 particles/ml) for 24 hours. After the incubation, media were replaced with particle-free media and MTT (5 mg/ml) solutions and incubated for 3 hours at 37°C in 5% CO_2. Next, the media were removed, and then insoluble formazans were dissolved by dimethyl sulfoxide. Intensity changes at 540 nm corresponding to the absorption peak of formazan were obtained through a benchmark microplate reader (Bio-Rad).

Analysis of distribution of LGNP in the single cell
H. sapiens brain glioblastoma U-87MG cells (2×10^5) were seeded in a 1×1–mm chambered glass substrate and incubated overnight to allow cell attachment. Nanoparticles (10^8) with a diameter of 100 nm, LGNP (derived from measured absorbance spectrum compared with GNP) and GNP (BBI Solutions), were applied to each cell chamber and incubated for 12 hours and fixed with formaldehyde, and gold spectrum intensity was measured by LSM 710 confocal microscopy (Carl Zeiss). The *xyz* scanning range for the confocal microscopy was 212 μm, 212 μm, and 20 μm³ based on a 40× water objective lens; 21 to 40 stacks with 1.0-μm interval were measured to obtain a 3D image. HeNe laser (543 nm) was used as an excitation wavelength, and emission windows were set at 548 to 671 nm for the gold spectrum. The ZEN 2012 software (Carl Zeiss) was used to acquire the gold spectrum.

Intracellular imaging via SERS
The Raman spectrum and image were measured by NTEGRA Spectra (NT-MDT) equipped with a liquid nitrogen–cooled CCD (charge-coupled device) detector and an inverted optical microscope (Olympus IX71). The *xyz* scanning range was 50 μm, 50 μm, and 6 mm³, and the resolution of the spectrometer in the *xy* plane was 200 to 500 nm along the *z* axis. The signals were obtained by a near-infrared laser that emitted light at a 785-nm wavelength, with an irradiation laser power of 3 mW on the sample plane controlled by a neutral density filter. Spots (32×32) per 50×50–μm² scan area were exposed for 1 s for each spot,

and the signal between 400 and 1600 cm^{-1} was measured as the Raman spectrum and imaging. A blank spectrum was acquired before each step, which allowed the absorbance to be subsequently measured.

SUPPLEMENTARY MATERIALS
Supplementary material for this article is available at http://advances.sciencemag.org/cgi/content/full/2/12/e1601838/DC1
Simulation details
fig. S1. Schematic illustration of conventional approaches for liposome/metal hybrids and their critical limitations.
fig. S2. Additional TEM images of LGNP (using membrane filter with a pore diameter of 100 nm).
fig. S3. Photographs and absorbance spectra of control experiments.
fig. S4. Reduction of gold ions above the transition temperature of lipid (DSPC).
fig. S5. Molecular structure of DSPC and EDS spectrum and relative atomic percentages of as-prepared liposome/Au and liposome/Ag hybrid nanoparticles.
fig. S6. Time-dependent representative absorbance spectra of programmable liposome solution after the exposure with gold precursor.
fig. S7. Diffusivities of acetamide and neutral gold ion complex.
fig. S8. Photographs and absorbance spectra of solutions of the gold precursor–encoded liposome after addition of reducing agent.
fig. S9. Additional TEM images of various liposome/metal hybrid nanoparticles.
fig. S10. Representative time-resolved absorbance spectra of liposome/monometallic hybrid nanoparticle.
fig. S11. Size distributions of liposome/monometallic and liposome/bimetallic hybrids.
fig. S12. EDS spectra of liposome/bimetallic hybrids.
fig. S13. Representative TEM images and corresponding EDS elemental line profiles of liposome/bimetallic hybrids.
fig. S14. Representative TEM images of liposome/bimetallic hybrids synthesized from different precursor molar ratios.
fig. S15. Atomic percentages and absorbance spectra of liposome/Au-Ag hybrids and liposome/Au-Pd hybrids synthesized from different precursor molar ratios.
fig. S16. Representative relative absorbance at the SPR peaks of LGNP, GNP, and GNR under a wide variety of biologically relevant solutions and representative relative absorbance of LGNP with time duration of up to 1 month.
fig. S17. Viability of U-87 MG cells treated with LGNP and GNP solutions.
fig. S18. Optical microscope images and Raman spectra obtained from various cells after being treated with LGNP and GNP.
fig. S19. Fluorescent image and Raman spectra obtained from Alexa Fluor 546–stained U-87 MG cells, and optical microscope images and Raman maps obtained from Alexa Fluor 546–stained U-87MG cells after being treated with LGNP and GNP.
table S1. Calculated relative atomic percentages of gold and oxygen atoms in LGNP.
table S2. The number of metal atoms per unit volume in liposome/Au, liposome/Ag, and liposome/Pd hybrids, measured by inductively coupled plasma atomic emission spectroscopy.
Reference (*51*)

REFERENCES AND NOTES
1. R. R. Arvizo, S. Bhattacharyya, R. A. Kudgus, K. Giri, R. Bhattacharya, P. Mukherjee, Intrinsic therapeutic applications of noble metal nanoparticles: Past, present and future. *Chem. Soc. Rev.* **41**, 2943–2970 (2012).
2. A. S. Thakor, J. Jokerst, C. Zavaleta, T. F. Massoud, S. S. Gambhir, Gold nanoparticles: A revival in precious metal administration to patients. *Nano Lett.* **11**, 4029–4036 (2011).
3. E. Y. Lukianova-Hleb, Y.-S. Kim, I. Belatsarkouski, A. M. Gillenwater, B. E. O'Neill, D. O. Lapotko, Intraoperative diagnostics and elimination of residual microtumours with plasmonic nanobubbles. *Nat. Nanotechnol.* **11**, 525–532 (2016).
4. A. K. Rengan, A. B. Bukhari, A. Pradhan, R. Malhotra, R. Banerjee, R. Srivastava, A. De, In vivo analysis of biodegradable liposome gold nanoparticles as efficient agents for photothermal therapy of cancer. *Nano Lett.* **15**, 842–848 (2015).
5. Y. Wang, C. Dai, X.-P. Yan, Fabrication of folate bioconjugated near-infrared fluorescent silver nanoclusters for targeted in vitro and in vivo bioimaging. *Chem. Commun.* **50**, 14341–14344 (2014).
6. K. A. Homan, M. Souza, R. Truby, G. P. Luke, C. Green, E. Vreeland, S. Emelianov, Silver nanoplate contrast agents for in vivo molecular photoacoustic imaging. *ACS Nano* **6**, 641–650 (2012).
7. M. Manikandan, N. Hasan, H.-F. Wu, Platinum nanoparticles for the photothermal treatment of Neuro 2A cancer cells. *Biomaterials* **34**, 5833–5842 (2013).
8. C. Wang, X. Cai, J. Zhang, X. Wang, Y. Wang, H. Ge, W. Yan, Q. Huang, J. Xiao, Q. Zhang, Y. Cheng, Trifolium-like platinum nanoparticle-mediated photothermal therapy inhibits tumor growth and osteolysis in a bone metastasis model. *Small* **11**, 2080–2086 (2015).

9. X. Huang, S. Tang, X. Mu, Y. Dai, G. Chen, Z. Zhou, F. Ruan, Z. Yang, N. Zheng, Freestanding palladium nanosheets with plasmonic and catalytic properties. *Nat. Nanotechnol.* **6**, 28–32 (2011).

10. A. J. McGrath, Y.-H. Chien, S. Cheong, D. A. J. Herman, J. Watt, A. M. Henning, L. Gloag, C.-S. Yeh, R. D. Tilley, Gold over branched palladium nanostructures for photothermal cancer therapy. *ACS Nano* **9**, 12283–12291 (2015).

11. J. Tang, X. Jiang, L. Wang, H. Zhang, Z. Hu, Y. Liu, X. Wu, C. Chen, Au@Pt nanostructures: A novel photothermal conversion agent for cancer therapy. *Nanoscale* **6**, 3670–3678 (2014).

12. H. Jang, D.-H. Min, Spherically-clustered porous Au–Ag alloy nanoparticle prepared by partial inhibition of galvanic replacement and its application for efficient multimodal therapy. *ACS Nano* **9**, 2696–2703 (2015).

13. T. L. Moore, L. Rodriguez-Lorenzo, V. Hirsch, S. Balog, D. Urban, C. Jud, B. Rothen-Rutishauser, M. Lattuada, A. Petri-Fink, Nanoparticle colloidal stability in cell culture media and impact on cellular interactions. *Chem. Soc. Rev.* **44**, 6287–6305 (2015).

14. E. C. Cho, Q. Zhang, Y. Xia, The effect of sedimentation and diffusion on cellular uptake of gold nanoparticles. *Nat. Nanotechnol.* **6**, 385–391 (2011).

15. W. G. Kreyling, A. M. Abdelmonem, Z. Ali, F. Alves, M. Geiser, N. Haberl, R. Hartmann, S. Hirn, D. J. de Aberasturi, K. Kantner, G. Khadem-Saba, J.-M. Montenegro, J. Rejman, T. Rojo, I. R. de Larramendi, R. Ufartes, A. Wenk, W. J. Parak, In vivo integrity of polymer-coated gold nanoparticles. *Nat. Nanotechnol.* **10**, 619–623 (2015).

16. X. Liu, J. Cao, H. Li, J. Li, Q. Jin, K. Ren, J. Ji, Mussel-inspired polydopamine: A biocompatible and ultrastable coating for nanoparticles in vivo. *ACS Nano* **7**, 9384–9395 (2013).

17. P. P. Pillai, S. Huda, B. Kowalczyk, B. A. Grzybowski, Controlled pH stability and adjustable cellular uptake of mixed-charge nanoparticles. *J. Am. Chem. Soc.* **135**, 6392–6395 (2013).

18. Y.-C. Chung, I.-H. Chen, C.-J. Chen, The surface modification of silver nanoparticles by phosphoryl disulfides for improved biocompatibility and intracellular uptake. *Biomaterials* **29**, 1807–1816 (2008).

19. L. Zhang, L. Laug, W. Münchgesang, E. Pippel, U. Gösele, M. Brandsch, M. Knez, Reducing stress on cells with apoferritin-encapsulated platinum nanoparticles. *Nano Lett.* **10**, 219–223 (2010).

20. W. T. Al-Jamal, K. Kostarelos, Liposomes: From a clinically established drug delivery system to a nanoparticle platform for theranostic nanomedicine. *Acc. Chem. Res.* **44**, 1094–1104 (2011).

21. G. Von White II, Y. Chen, J. Roder-Hanna, G. B. Bothun, C. L. Kitchens, Structural and thermal analysis of lipid vesicles encapsulating hydrophobic gold nanoparticles. *ACS Nano* **6**, 4678–4685 (2012).

22. B. F. Leo, S. Chen, Y. Kyo, K.-L. Herpoldt, N. J. Terrill, I. E. Dunlop, D. S. McPhail, M. S. Shaffer, S. Schwander, A. Gow, J. Zhang, K. F. Chung, T. D. Tetley, A. E. Porter, M. P. Ryan, The stability of silver nanoparticles in a model of pulmonary surfactant. *Environ. Sci. Technol.* **47**, 11232–11240 (2013).

23. D. Zhu, Z. Wang, S. Zong, H. Chen, X. Wu, Y. Pei, P. Chen, X. Ma, Y. Cui, Ag@4ATP-coated liposomes: SERS traceable delivery vehicles for living cells. *Nanoscale* **6**, 8155–8161 (2014).

24. P. Nativo, I. A. Prior, M. Brust, Uptake and intracellular fate of surface-modified gold nanoparticles. *ACS Nano* **2**, 1639–1644 (2008).

25. G. Wu, A. Mikhailovsky, H. A. Khant, C. Fu, W. Chiu, J. A. Zasadzinski, Remotely triggered liposome release by near-infrared light absorption via hollow gold nanoshells. *J. Am. Chem. Soc.* **130**, 8175–8177 (2008).

26. J. Nam, Y. S. Ha, S. Hwang, W. Lee, J. Song, J. Yoo, S. Kim, pH-responsive gold nanoparticles-in-liposome hybrid nanostructures for enhanced systemic tumor delivery. *Nanoscale* **5**, 10175–10178 (2013).

27. T. Lajunena, L. Viitalab, L.-S. Kontturia, T. Laaksonena, H. Liangc, E. Vuorimaa-Laukkanenc, T. Viitalaa, X. L. Guéveld, M. Yliperttulaa, L. Murtomäkib, A. Urttia, Light induced cytosolic drug delivery from liposomes with gold nanoparticles. *J. Controlled Release* **203**, 85–98 (2015).

28. M. R. Rasch, E. Rossinyol, J. L. Hueso, B. W. Goodfellow, J. Arbiol, B. A. Korgel, Hydrophobic gold nanoparticle self-assembly with phosphatidylcholine lipid: Membrane-loaded and Janus vesicles. *Nano Lett.* **10**, 3733–3739 (2010).

29. D. Pornpattananangkul, S. Olson, S. Aryal, M. Sartor, C.-M. Huang, K. Vecchio, L. Zhang, Stimuli-responsive liposome fusion mediated by gold nanoparticles. *ACS Nano* **4**, 1935–1942 (2010).

30. H.-Y. Lee, S. H. R. Shin, L. L. Abezgauz, S. A. Lewis, A. M. Chirsan, D. D. Danino, K. J. M. Bishop, Integration of gold nanoparticles into bilayer structures via adaptive surface chemistry. *J. Am. Chem. Soc.* **135**, 5950–5953 (2013).

31. E. M. Curtis, A. H. Bahrami, T. R. Weikl, C. K. Hall, Modeling nanoparticle wrapping or translocation in bilayer membranes. *Nanoscale* **7**, 14505–14514 (2015).

32. B. Y. Moghadam, W.-C. Hou, C. Corredor, P. Westerhoff, J. D. Posner, Role of nanoparticle surface functionality in the disruption of model cell membranes. *Langmuir* **28**, 16318–16326 (2012).

33. L. Zhang, S. Granick, How to stabilize phospholipid liposomes (using nanoparticles). *Nano Lett.* **6**, 694–698 (2006).

34. D. V. Volodkin, A. G. Skirtach, H. Möhwald, Near-IR remote release from assemblies of liposomes and nanoparticles. *Angew. Chem. Int. Ed.* **48**, 1807–1809 (2009).

35. D. Marsh, *CRC Handbook of Lipid Bilayers* (CRC Press, 1990).

36. D. D. Lasic, Y. Barenholz, *Handbook of Nonmedical Applications of Liposomes: Theory and Basic Sciences* (CRC Press, 1996).

37. F. Moreau, G. C. Bond, A. O. Taylor, Gold on titania catalysts for the oxidation of carbon monoxide: Control of pH during preparation with various gold contents. *J. Catal.* **231**, 105–114 (2005).

38. S.-J. Marrink, H. J. C. Berendsen, Simulation of water transport through a lipid membrane. *J. Phys. Chem.* **98**, 4155–4168 (1994).

39. D. Bemporad, J. W. Essex, C. Luttmann, Permeation of small molecules through a lipid bilayer: A computer simulation study. *J. Phys. Chem. B* **108**, 4875–4884 (2004).

40. K. Takiyama, Formation and aging of precipitates. VIII. Formation of monodisperse particles (1) gold sol particles by sodium citrate method. *Bull. Chem. Soc. Jpn.* **31**, 944–950 (1958).

41. S. K. Cha, J. H. Mun, T. Chang, S. Y. Kim, J. Y. Kim, H. M. Jin, J. Y. Lee, J. Shin, K. H. Kim, S. O. Kim, Au–Ag core–shell nanoparticle array by block copolymer lithography for synergistic broadband plasmonic properties. *ACS Nano* **9**, 5536–5543 (2015).

42. J.-S. Jang, S.-J. Kim, S.-J. Choi, N.-H. Kim, M. Hakim, A. Rothschildc, I.-D. Kim, Thin-walled SnO₂ nanotubes functionalized with Pt and Au catalysts via the protein templating route and their selective detection of acetone and hydrogen sulfide molecules. *Nanoscale* **7**, 16417–16426 (2015).

43. R. R. Juluri, A. Rath, A. Ghosh, A. Bhukta, R. Sathyavathi, D. Narayana Rao, K. Müller, M. Schowalter, K. Frank, T. Grieb, F. Krause, A. Rosenauer, P. V. Satyam, Coherently embedded Ag nanostructures in Si: 3D imaging and their application to SERS. *Sci. Rep.* **4**, 4633 (2014).

44. J.-M. Yan, Z.-L. Wang, L. Gu, S.-J. Li, H.-L. Wang, W.-T. Zheng, Q. Jiang, AuPd–MnOₓ/MOF–graphene: An efficient catalyst for hydrogen production from formic acid at room temperature. *Adv. Energy Mater.* **5**, 1500107 (2015).

45. R. Nie, J. Wang, L. Wang, Y. Qin, P. Chen, Z. Hou, Platinum supported on reduced graphene oxide as a catalyst for hydrogenation of nitroarenes. *Carbon* **50**, 586–596 (2012).

46. Q.-L. Zhanga, K.-J. Ju, X.-Y. Huang, A.-J. Wang, J. Wei, J.-J. Feng, Metformin mediated facile synthesis of AuPt alloyed nanochains with enhanced electrocatalytic properties for alcohol oxidation. *Electrochim. Acta* **182**, 305–311 (2015).

47. H.-J. Jang, S. Hong, S. Ham, K. L. Shuford, S. Park, Site-specific growth of a Pt shell on Au nanoplates: Tailoring their surface plasmonic behavior. *Nanoscale* **6**, 7339–7345 (2014).

48. C. Gao, Y. Hu, M. Wang, M. Chi, Y. Yin, Fully alloyed Ag/Au nanospheres: Combining the plasmonic property of Ag with the stability of Au. *J. Am. Chem. Soc.* **136**, 7474–7479 (2014).

49. A. Sánchez-Iglesias, M. Grzelczak, T. Altantzis, B. Goris, J. Pérez-Juste, S. Bals, G. V. Tendeloo, S. H. Donaldson Jr., B. F. Chmelka, J. N. Israelachvili, L. M. Liz-Marzán, Hydrophobic interactions modulate self-assembly of nanoparticles. *ACS Nano* **6**, 11059–11065 (2012).

50. V. V. Breus, C. D. Heyes, K. Tron, G. U. Nienhaus, Zwitterionic biocompatible quantum dots for wide pH stability and weak nonspecific binding to cells. *ACS Nano* **3**, 2573–2580 (2009).

51. A. Einstein, *Investigations on the Theory of the Brownian Movement* (Courier Corporation, 1956).